# Intracellular pH dynamics respond to microenvironment stiffening and mediate vasculogenic mimicry through β-catenin

**Leah M. Lund[1,2], Angelina N. Marchi[1,2], Laura Alderfer[3,5], Eva Hall[3], Jacob Hammer[1,2], Keelan J. Trull[1,2], Donny Hanjaya-Putra[2,3,4] and Katharine A. White[1,2]**

[1]Department of Chemistry and Biochemistry, University of Notre Dame
251 Nieuwland Science Hall
Notre Dame, IN 46556 USA

[2]Harper Cancer Research Institute, University of Notre Dame
1234 N. Notre Dame Avenue
South Bend, IN 46617 USA

[3]Bioengineering Graduate Program, Aerospace and Mechanical Engineering, University of Notre Dame
153 Multidisciplinary Engineering Research Building
Notre Dame, IN 46556 USA

[4]Chemical and Biomolecular Engineering, University of Notre Dame
250 Nieuwland Hall
Notre Dame, IN 46556 USA

[5]Current: Vivodyne
Suite 775 601 Walnut Street
Philadelphia PA 19106 USA

## Abstract

Dysregulated intracellular pH (pHi) dynamics and an altered tumor microenvironment have emerged as drivers of cancer cell phenotypes. However, the molecular integration between the physical properties of the microenvironment and dynamic intracellular signaling responses remains unclear. Here, we use two metastatic cell models, one breast and one lung, to assess pHi response to varying extracellular matrix (ECM)

stiffness. To experimentally model ECM stiffening, we use two tunable-stiffness hydrogel systems: Matrigel and hyaluronic acid (HA) gels, which mimic the increased protein secretion and crosslinking associated with ECM stiffening. We find that single-cell pHi decreases with increased ECM stiffness in both hydrogel systems and both metastatic cell types. We also observed that stiff ECM promotes vasculogenic mimicry (VM), a phenotype associated with metastasis and resistance. Importantly, we show that decreased pHi is both a necessary and sufficient mediator of VM, as raising pHi on stiff ECM reduces VM phenotypes and lowering pHi on soft ECM drives VM. We characterize β-catenin as a pH-dependent molecular mediator of pH-dependent VM, where stiffness-driven changes in β-catenin abundance can be overridden by increased pHi. We uncover a dynamic relationship between matrix stiffness and pHi, thus suggesting pHi dynamics can override mechanosensitive cell responses to the extracellular microenvironment.

## Introduction

The extracellular matrix (ECM) is a protein-rich structure that becomes dysregulated in cancer, driving cancer cell adaptation and promotion of cancer cell phenotypes[1]. This increasingly rigid and dense tumor ECM has been shown to promote cancer cell invasion and vasculogenic mimicry, an adaptive cancer phenotype [2,3]. In addition to the dysregulated extracellular environment, cancer cells also experience dysregulated pH dynamics[4], with increased intracellular pH (pHi) (>7.4) and decreased extracellular pH (pHe) (<7.2) compared to normal epithelial cells (pHi 7.0-7.3; pHe 7.4)[5]. This reversal of the pH gradient is an early event in cellular transformation[6] and has

57 been directly linked to adaptive changes in cancer cell signaling, metabolism,
58 proliferation, and evasion of apoptosis[5].

59 Increased ECM stiffness promotes various cancer cell phenotypes including
60 increased hypoxia[7], vasculogenic mimicry[8], cell durotaxis[9], and selection for tumor
61 initiating cell (TIC) or cancer stem-cell phenotypes[4,10–13]. Importantly, many equivalent
62 or similar processes are also linked to dysregulated pHi dynamics including hypoxia[11],
63 cell invasion[4], and maintenance of a stem-like phenotype in adult and embryonic stem
64 cell models[14]. However, the molecular mechanisms that integrate the physical
65 properties of the microenvironment with intracellular cancer cell signaling response are
66 largely unknown.

67 While prior work has shown pHi dynamics can directly regulate normal
68 mechanosensitive behaviors including focal adhesion remodeling[15] and epithelial cell-
69 cell contacts[16,17], there are significant gaps in knowledge of the molecular crosstalk
70 between ECM stiffening and pHi dynamics in cancer cells. One limitation is technical: it
71 is challenging to develop mechanically tunable model systems that mimic physiological
72 ECM dysregulation with suitable mechanical control. Previous studies have used
73 synthetic ECM models, including Matrigel/Geltrex[18] and Hyaluronan[19] based systems.
74 However, these studies have lacked the ability to decouple the contributions of ECM
75 protein abundance and ECM crosslinking density as independent drivers of
76 mechanosensitive cell responses.

77 Another limiting factor in characterizing molecular links between ECM stiffness
78 and pHi is that most mechanistic studies of how pHi dynamics regulate cell behaviors
79 are performed under non-physiological culture conditions and lack single-cell resolution.

These limitations apply to most studies of pHi dynamics in biology, but are compounded when exploring effects of physical forces on cellular pHi dynamics and in the context of phenotypically heterogeneous cancer cells.

Here, we pair synthetic tunable-stiffness ECM models with live-cell pHi measurements and non-invasive pHi manipulation to elucidate how pHi dynamics respond to ECM stiffening. We further explore a mechanistic role of pHi in regulating a cancer-associated mechanosensitive phenotype called vasculogenic mimicry (VM). We use two unique synthetic matrix models to mimic ECM stiffening through increasing protein abundance (Matrigel/Geltrex) and crosslinking density (hyaluronic acid gels), and measure single-cell pHi in metastatic breast and lung cancer cells. We show that pHi decreases with increased stiffness using both matrix models. We also show that cells plated on stiff ECM acquire distinct VM phenotypes that can be modulated by dynamically altering pHi. Importantly, raising pHi in cells plated on stiff matrix reduces VM phenotypes while lowering pHi in cells plated on soft matrix induces acquisition of a stiffness-independent VM phenotype. We also investigate the pH dependence of two molecular regulators of VM that have been previously shown to be regulated by ECM stiffness (β-catenin and FOXC2). We show that β-catenin is a pH-dependent mediator of VM phenotype while FOXC2 activity is pHi insensitive in this system. This suggests β-catenin as a novel necessary regulator of pH-dependent vasculogenic mimicry. Overall, our work reveals a previously unidentified link between mechanosensing and pHi dynamics in cancer and further suggests low pHi as a necessary and sufficient mediator of VM, a phenotype associated with aggressive cancers.

## Results

### Stiffening extracellular matrix lowers pHi in metastatic human lung carcinoma

Increased tumor microenvironment (TME) stiffness can be caused by increased ECM protein deposition and increased crosslinking[20] (Figure 1A). To investigate the central hypothesis of how a stiffening extracellular environment alters pHi, we used two tunable-stiffness hydrogel models to control ECM stiffness with high specificity and using two unique modes of mechanical modulation. To mimic the effects of ECM stiffness changes resulting from altered ECM protein crosslinking, we used a hyaluronic-acid (HA) gel system where variable crosslinking density tunes ECM stiffness independent of protein concentration and composition[21,22]. HA is a non-sulfated linear polysaccharide of (1-β-4)d-glucuronic acid and (1-β-3)N-acetyl-d-glucosamine, and is a ubiquitous component of the ECM[19]. HA is particularly abundant in the extracellular environment of the lung and brain[19], and increased HA secretion is associated with cancers[19] as well as fibrotic diseases of the liver and lung[23].

Recent work has shown that HA can be functionalized to contain thiol-reactive cross-linkable regions, with increased crosslinking adding rigidity to the ECM allowing tunable stiffness[24]. Our HA gel tunable-stiffness model consists of a uniform mixture of gelatin and thiol-modified hyaluronan across stiffnesses, while stiffness is controlled by modulating amounts (%) of thiol-reactive PEGDA crosslinker (see methods for details). The HA gel model consists of four levels of crosslinking agent mimicking ECM stiffness changes induced by increased protein crosslinking and has a previously reported tunable stiffness range from ~100-1500 Pa[25] (Figure 1B). This system allows us to modulate matrix stiffness by adjusting the extent of ECM protein crosslinking while

126 maintaining a consistent concentration of matrix components (hyaluronan and gelatin)
127 across all stiffness conditions. This ability to model ECM stiffness independent of matrix
128 concentration is a unique feature which provides advantage over model systems which
129 use natural hydrogels in decoupling individual drivers of ECM stiffening.

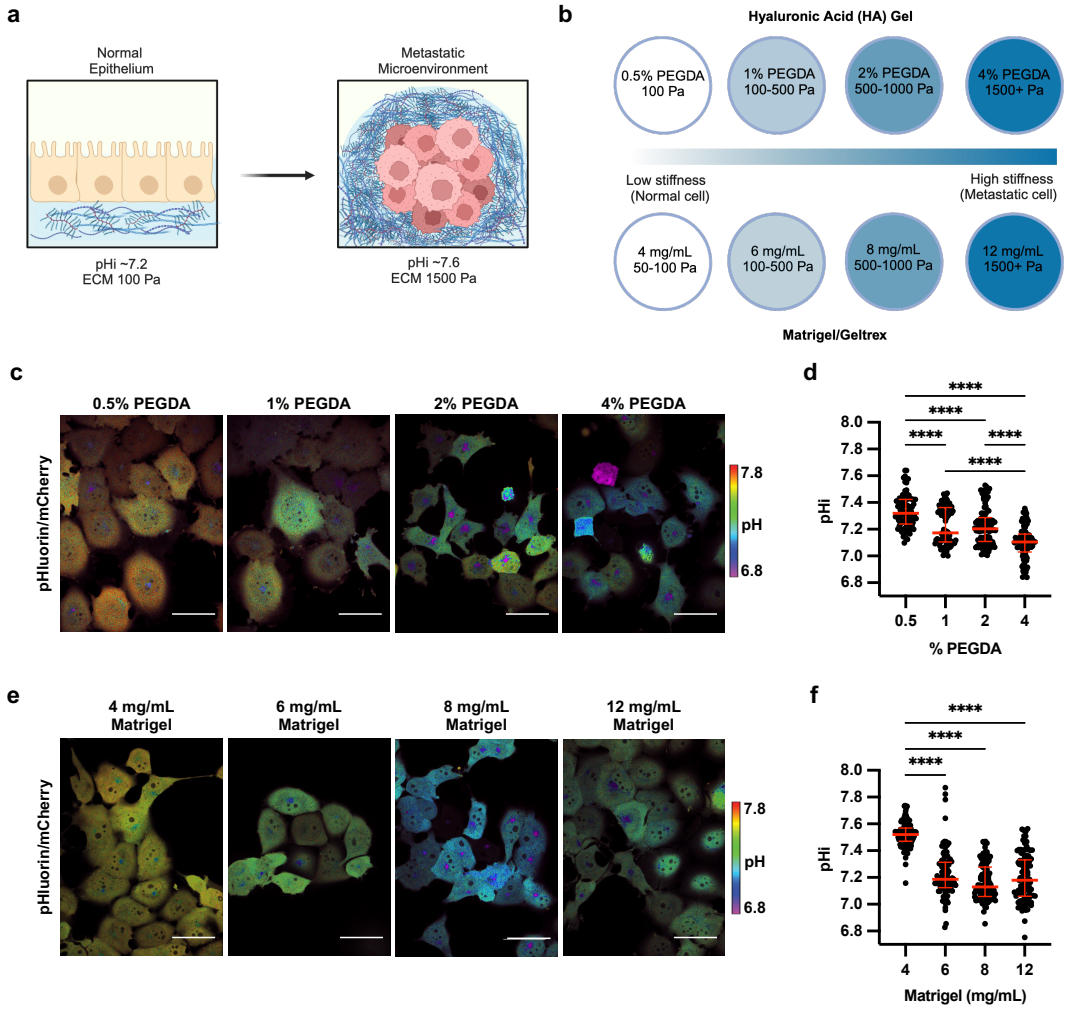


130

131 **Figure 1: Stiffening extracellular matrix lowers pHi in metastatic human lung**
132 **carcinoma (H1299). a)** Schematic of increased pHi and ECM stiffening (via increased
133 protein secretion and increased protein crosslinking) associated with tumorigenesis. **b)**
134 Schematic of synthetic ECM models with tunable-stiffness (~50 Pa-1,500 Pa). The
135 Matrigel (or Geltrex) model mimics increased ECM protein secretion while hyaluronic
136 acid (HA) gel system mimics increased ECM protein crosslinking. **c)** Representative
137 images of H1299 cells stably expressing mCherry-pHluorin pH biosensor plated on
138 varying HA gel stiffnesses. Images show ratiometric display of pHluorin/mCherry
139 fluorescence. Scale bars: 50 μm. **d)** Quantification of single-cell pHi data collected as

shown in (c). (n=3 biological replicates; n=91 0.5% PEGDA, n=90 1% PEGDA, n=102 2% PEGDA, n=89 4% PEGDA. Red lines show medians ± IQR). **e)** Representative images of H1299 cells stably expressing mCherry-pHluorin pH biosensor plated on varying Matrigel stiffnesses. Images show ratiometric display of pHluorin/mCherry fluorescence. Scale bars: 50 µm. **f)** Quantification of single-cell pHi data collected as shown in (e). (n=3 biological replicates; n=93 4mg/mL, n=92 6mg/mL, n=102 8mg/mL, n=97 12mg/mL. Red lines show medians ± IQR). For (d) and (f), significance was determined by a Kruskal-Wallis test (****P<0.0001).

To mimic the effects of stiffness changes due to increased ECM protein secretion, we used a Matrigel- or Geltrex-based tunable-stiffness gel system. Matrigel and Geltrex are naturally-derived matrices that mimic the tumor microenvironment of stromal-rich tissues, such as breast, lung, and prostate[26]. The Matrigel and Geltrex commercial matrix mixtures are rich in laminin and collagen; EMC proteins that directly promote integrin signaling[27]. Varying the concentration of Matrigel and Geltrex effectively titrates ECM protein concentrations[28], mimicking the increased secretion of ECM proteins associated with stiffening tumor microenvironment[29]. We used tunable-stiffness Matrigel/Geltrex models that consist of four Matrigel/Geltrex concentrations (4 mg/mL-12 mg/mL) with stiffness ranges of ~50-1,500 Pa[30–32] (Figure 1B). For these stiffness determinations, the manufacturer reports an elastic modulus (G′) that can be converted to Young's modulus (matrix stiffness) using the following equation E= 2G'(1 + v). Prior work has indicated that hydrogels can be assumed to be incompressible, such that their Poisson's ratio (v) approaches 0.5[33], simplifying the equation to E=3G' Importantly, in the Matrigel/Geltrex tunable-stiffness gel systems, as the ECM protein concentrations increase, so does the available ligand concentration for integrin-mediated interactions. This gel model allows us to assess effects of ECM stiffening on pHi when intracellular integrin signaling is also titrating.

167 With the two tunable-stiffness hydrogel systems established, we next selected
168 cancer cell lines that originated from tissues with a relatively soft ECM, such as lung
169 and breast, where tumorigenic ECM stiffening has been associated with both increased
170 metastasis and invasion[26]. We have previously established and characterized single-cell
171 pHi heterogeneity in a clonal metastatic lung cancer cell line (H1299) and a clonal
172 breast cancer cell line (MDA-MB-231), all plated and imaged on glass[34]. We have
173 engineered these cell lines to stably express a genetically-encoded ratiometric pH
174 biosensor mCherry-pHluorin (mCh-pHl)[34]. This biosensor is a fusion of the fluorescent
175 protein pHluorin (pKa 7.1) that is pH-sensitive in the physiological range, and the
176 fluorescent protein mCherry, that is pH-insensitive in the physiological range[35]. For
177 accurate pHi measurements in single cells, ratiometric imaging of pHluorin and mCherry
178 fluorescence can be performed followed by single-cell standardization using isotonic
179 buffers with a known pHi containing the protonophore Nigericin to equilibrate
180 intracellular and extracellular (buffer) pH[36]. Single-cell standard curves are then
181 generated, enabling back-calculation of pHi from pHluorin and mCherry fluorescence
182 intensity ratios (Supplemental Figure 1, see methods for details). This biosensor has
183 successfully been used in prior studies to measure single-cell spatiotemporal pHi
184 dynamics in clonal cancer and normal epithelial cell populations without affecting cell
185 morphology or behavior[15,34,35].
186 To determine effects of altered ECM stiffness on pHi, we cultured H1299 cells
187 expressing the mCh-pHl biosensor on matrix-coated imaging dishes for 48 hours. This
188 incubation allowed for cells to adhere and respond to the varied stiffness of each matrix
189 system. In cells plated on HA gels, single-cell pHi decreased with increasing stiffness

190 (Figure 1D). Cells plated on the stiffest matrix (4% PEGDA) had a significantly
191 decreased pHi (Figure 1D; 7.10±0.07; median±interquartile range (IQR)) compared to
192 cells on the softest matrix (0.5% PEGDA) (Figure 1D; 7.32±0.10; median±IQR). We also
193 observed that intermediate ECM stiffnesses (1% PEGDA and 2% PEGDA) produced
194 intermediate effects on pHi, with a stepwise trend of decreasing pHi with increasing
195 stiffness (Figure 1F; 2% PEGDA 7.20±0.10; 1% PEGDA 7.17±0.19; medians±IQR). The
196 overall decrease in pHi of ~0.2 pH units between soft and stiff ECM is within the range
197 of physiological pHi dynamics that have been shown to regulate normal cell behaviors
198 including cell cycle progression[34], differentiation[13,37], and migration[38]. This result shows
199 that stiffening of the ECM through changes in protein crosslinking drives significant
200 decreases in single-cell pHi of clonal metastatic lung cancer cells. These data suggest
201 that progressive changes in ECM stiffness within the physiological range of normal to
202 metastatic mechanical stiffness environments can alter pHi in metastatic cancer cells,
203 suggesting a potential role for pHi in mechanosensitive cancer cell signaling and
204 behaviors.

205 We next determined whether the stiff ECM decreased pHi using the Matrigel
206 tunable-stiffness models, where ECM protein concentration is the predominant driver of
207 altered stiffness. In cells plated on varied Matrigel stiffnesses, single-cell pHi decreased
208 with increasing stiffness (Figure 1E). Cells plated on the stiffest matrix (12 mg/mL) had
209 a significantly decreased pHi (7.18±0.15; median±IQR) compared to the softest matrix
210 (4 mg/mL; 7.52±0.49; median±IQR) (Figure 1F). The decrease in pHi of ~0.35 units
211 between stiffest (~1,500 Pa) and softest (~50 Pa) ECM in this system is also consistent
212 with the pHi changes we measured between stiffest and softest HA gel models.

213 However, in the Matrigel tunable-stiffness model system, the pHi measured on
214 intermediate stiffnesses (6 mg/mL Matrigel, 7.19±0.13; 8 mg/mL Matrigel, 7.13±0.14;
215 medians±IQR) was not significantly different from the pHi of cells plated on a stiff matrix
216 (Figure 1F). This result shows that ECM stiffening decreases pHi in metastatic cells via
217 both increased ECM protein abundance and crosslinking, showing mechanism
218 independent ECM stiffness driven pHi dynamics in metastatic cells.
219 We next confirmed that ECM stiffness leads to decreased pHi using metastatic
220 breast epithelial cell model (MDA-MB-231) as another metastatic cell model derived
221 from a stromal-rich environment. The pHi of MDA-MB-231 cells was decreased by ~0.2
222 units in cells plated on a stiff matrix compared to soft matrix in both the Matrigel (soft
223 7.40±0.14; stiff 7.20±0.13; median±IQR) and HA gel (soft 7.43±0.14; stiff 7.28±0.10;
224 median±IQR) models (Supplemental Figure 1). Taken together, these data show that
225 increases in ECM stiffness mediated by either increased crosslinking (HA gel model) or
226 by increased ECM protein secretion (Matrigel model) both decrease pHi at the single-
227 cell level. Our data also show that the stiffness-dependent decreases in pHi are not
228 tissue specific as both breast and lung metastatic models exhibited a 0.2-0.35 decrease
229 in pHi on stiff compared to soft matrices. In summary, these data show that there is an
230 inverse relationship between ECM stiffening and pHi in these metastatic cancer cell
231 models, and further suggests a role for pHi in regulating pH-sensitive molecular
232 pathways to drive or reinforce stiffness-associated phenotypes.
233
234

235 **Stiffness dependent vasculogenic mimicry is reduced in high pHi conditions in**
236 **metastatic lung carcinoma**

237 When performing the single-cell pHi measurements on tunable-stiffness ECM
238 models, we also observed a distinct change in overall cancer cell morphology that
239 correlated with increased ECM stiffness. Metastatic cancer cells plated on soft matrix
240 grew in flat lawns of large rounded (H1299) or spindle-shaped cells (MDA-MB-231),
241 forming a near-confluent sheet. However, on stiff matrix, the metastatic cancer cells
242 grew in compact clusters of irregularly shaped cells, frequently exhibited 3D growth
243 phenotypes, and formed connected bridges of significantly elongated spindle shaped
244 cells between 3D "nodes" (Supplemental Figure 3). This change in cell morphology we
245 observed on stiff matrices has been previously described as a vasculogenic mimicry
246 (VM) phenotype. VM is an aggressive cancer phenotype observed both *in vivo* and *in*
247 *vitro*, where tumor cells organize into vessel-like structures, allowing nutrients and
248 oxygen access independent of traditional angiogenesis[39]. Previous studies have shown
249 increased ECM stiffness can drive VM[40] phenotypes and have also characterized 2D
250 VM phenotypes as a pronounced growth pattern where cells form distinct networks of
251 tightly packed cells with surrounding open space devoid of cell growth[41].

252 Our data showing single-cell pHi decreases in H1299 cells on stiff ECM led to the
253 hypothesis that low pHi is a necessary mediator of VM and that raising pHi in H1299
254 cells plated on stiff matrix would reduce the VM phenotype (Figure 2A). To directly test
255 this hypothesis, we established protocols to experimentally raise pHi in H1299 cells
256 plated on stiff ECM. Prior work showed that 50 mM Sodium Bicarbonate supplemented
257 into the media for 24 hours was sufficient to raise pHi in H1299 cells plated on glass[34].

258 We imaged single-cell pHi in H1299 cells plated on soft ECM, stiff ECM, and stiff ECM
259 with bicarbonate supplementation (Figure 2B). We found that bicarbonate significantly
260 increased pHi of cells plated on stiff ECM compared to untreated cells on stiff matrix
261 (stiff 7.27±0.08; stiff + Bicarbonate 7.43±0.08; median±IQR) (Figure 2C). While the
262 absolute pHi achieved with bicarbonate treatment on stiff HA gel matrix was lower than
263 the matched pHi of control cells plated on soft ECM (Figure 2C), the bicarbonate
264 treatment increased the pHi of cells plated on the stiffest ECM by approximately 0.2 pH
265 units (Figure 2C), which is similar to the magnitude of pHi changes we observed
266 between soft and stiff ECM across the various cell lines and gel systems.
267 We next tested the effects of increased pHi on the stiffness-dependent
268 vasculogenic mimicry phenotype. We found that H1299 cells acquired a vasculogenic
269 mimicry phenotype on stiff matrix, and this VM phenotype was abrogated when pHi was
270 increased on stiff matrix (Figure 2D). Cells plated on stiff matrix with bicarbonate-
271 induced increases in pHi grew in a 2D cobblestone-like morphology similar to the
272 morphology of cells grown on the soft ECM (Figure 2D, additional representative
273 images in Supplemental Figure 4). To confirm that the observed pH-dependent change
274 in cell morphology was not due to pH-dependent or stiffness-dependent differences in
275 cell proliferation, we assayed proliferation rates in H1299 cells plated on soft and stiff
276 ECM with and without increased pHi. Importantly, we did not observe any significant
277 differences in proliferation rates across our experimental conditions (Figure 2E). Our
278 data showing loss of VM networks when pHi is increased in cells plated on stiff ECM
279 demonstrate that low pHi is necessary to maintain VM phenotypes on stiff ECM.

280 Furthermore, these data show that high pHi can override stiffness-dependent

281 vasculogenic mimicry in a metastatic cancer model.

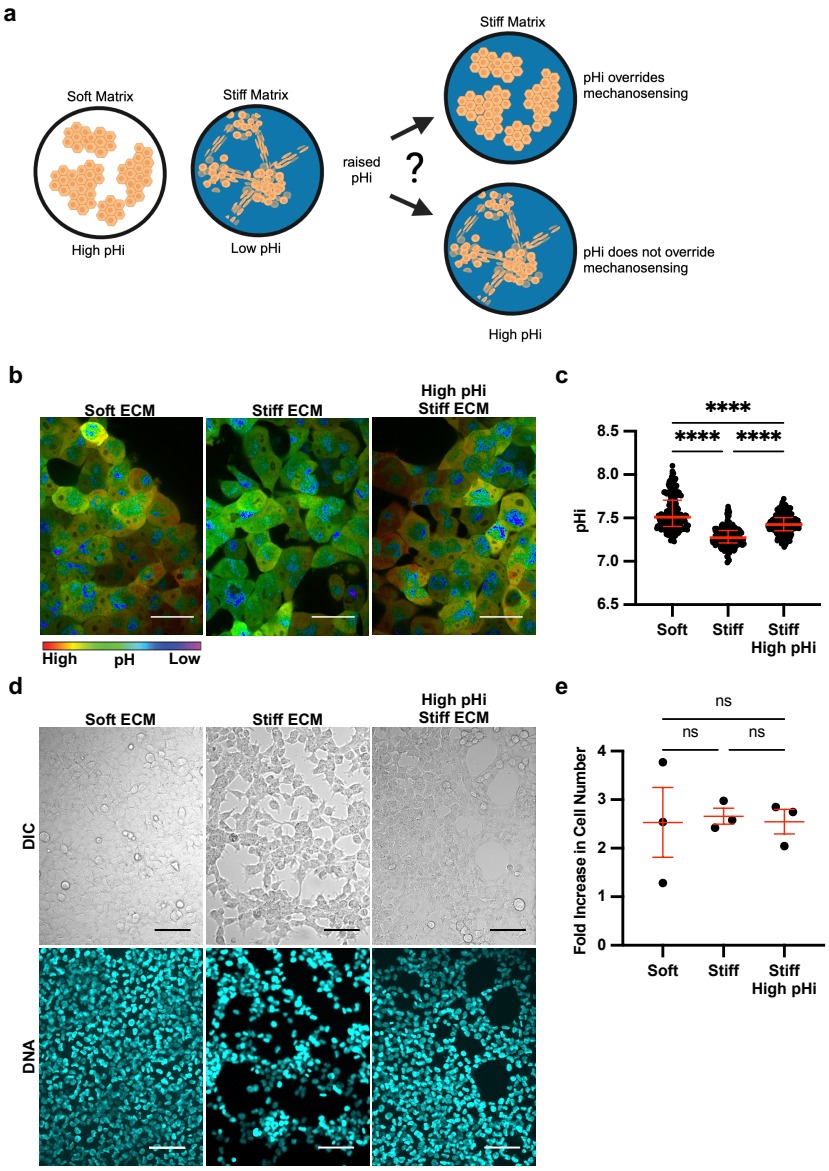


282

283 **Figure 2: Stiffness-dependent vasculogenic mimicry is reduced when pHi is**
284 **increased on stiff ECM. a)** Schematic of vasculogenic mimicry (VM) in 2D on stiffening
285 matrix. **b)** Representative images of H1299 cells stably expressing mCherry-pHluorin
286 pH biosensor plated on soft (0.5% PEGDA) and stiff (4% PEGDA) HA gels and stiff (4%
287 PEGDA) with raised pHi. Images show ratiometric display of pHluorin/mCherry
288 fluorescence ratios. Scale bars: 50 µm. **c)** Quantification of single-cell pHi data collected
289 as shown in (b) (n=3 biological replicates; n=201 soft, n=237 stiff, n=239 stiff high pHi.
290 Red lines show medians ± IQR). **d)** Representative images of H1299 cells plated on soft

(0.5% PEGDA) and stiff (4% PEGDA) HA gels. Images show differential interference contrast (DIC) and Hoechst stain (DNA, cyan). Scale bars: 100 μm. **e)** Quantification of cell proliferation across manipulation conditions. (n=3 biological replicates, n=9 per condition. Red lines show means ± SEM).

To quantify the observed stiffness- and pHi-dependent changes in cell morphology, we used a cell membrane marker and quantitative image analysis (see methods for details) pipeline to assess cell area (Figure 3A). Notably, single-cell area of H1299 cells was significantly lower in cells plated on stiff ECM compared to soft ECM (Figure 3B; stiff 338.6 $\mu m^2$±189; soft 406.5 $\mu m^2$±224.6; median±IQR). This result demonstrates that cell area is a robust quantitative morphology indicator that decreases with acquisition of VM phenotype on stiff ECM. This allows us to quantitatively distinguish cell morphologies corresponding to low VM and high VM conditions. Importantly, we found that cell area significantly increased (Figure 3C; 374.3 $\mu m^2$±210.6; median±IQR) when pHi was raised in H1299 cells plated on stiff ECM compared to control H1299 on stiff ECM (Figure 3B). This indicates that increased pHi attenuates the observed stiffness-dependent VM phenotype. The loss of VM networks and increased cell area when pHi is raised on stiff ECM demonstrates that low pHi is required for cells to acquire VM on stiff matrices. Together, our findings confirm previous literature characterizing vasculogenic mimicry as an ECM stiffness-mediated phenotype and further identifies decreased pHi as a previously unrecognized necessary regulator of VM.

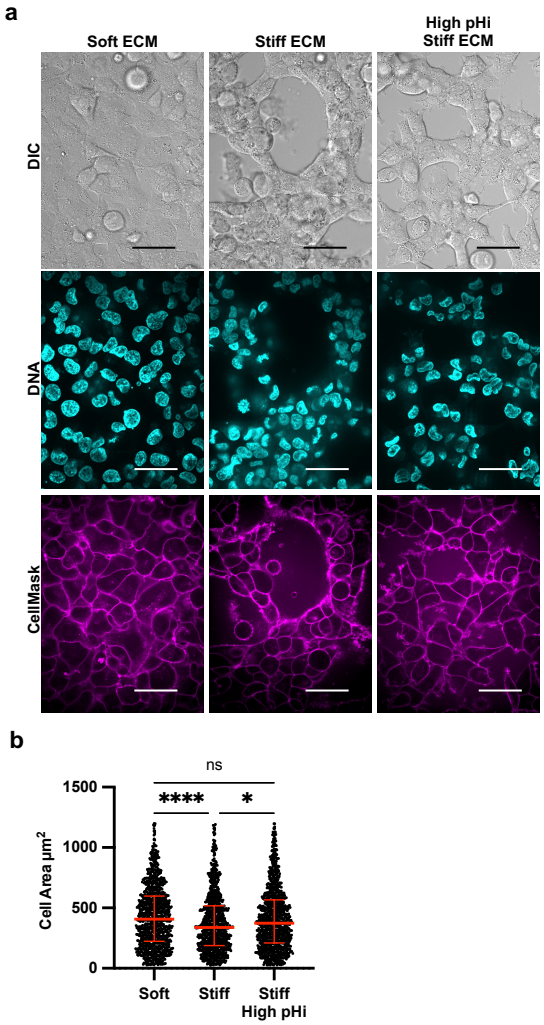


**Figure 3: Vasculogenic mimicry phenotype decreases cell area on stiff ECM, which is rescued by increasing pHi in metastatic lung carcinoma. a)** Representative images of H1299 cells plated on soft (0.5% PEGDA) and stiff (4% PEGDA) HA gels and stiff (4% PEGDA) with raised pHi. Images show differential interference contrast (DIC), Hoechst 33342 (DNA, cyan) and CellMask Deep Red membrane stain (Cy5, magenta). Scale bars: 50 µm. **b)** Quantification of single-cell area collected as shown in (a) (n=3 biological replicates, n=1061 soft, n=954 stiff, n=1078 stiff high pHi. Red lines show medians ± IQR).

**β-catenin abundance is stiffness-dependent, pHi-dependent, and necessary for stiffness-dependent vasculogenic mimicry**

We next investigated potential molecular drivers of pH-dependent regulation of VM. In epithelial cells, VM is regulated by several characterized mechanisms, including the activity and abundance of β-catenin[42,43]. β-catenin is a multifunctional protein involved in cell-cell adhesion and transcription. Previous work has shown that both whole cell abundance and transcriptional activity of β-catenin directly regulate VM[42]. A recent study using malignant melanoma cells showed that knockdown of β-catenin or silencing of its co-transcriptional activator transcription factor 4 (TCF4) disables VM phenotypes[42]. Additionally, previous work has shown that increased nuclear localization of β-catenin correlates with VM formation in colon cancer cells[43] and is associated with a stiffening ECM in liver cancer cells[44]. Importantly, ECM stiffening has also been shown to increase whole-cell β-catenin abundance in some cell lines, including human mesenchymal stem cells[45,46]. While previous studies have demonstrated the role of β-catenin in regulating VM, these studies have not characterized the cellular cues by which a stiff ECM increases β-catenin abundance or nuclear localization.

Our prior work has shown that high pHi reduces stability of β-catenin in normal canine kidney (MDCK) epithelial cells, leading to loss of β-catenin from adherens junctions[47]. More recently, we have shown that low pHi stabilizes β-catenin and increases the transcriptional activity in MDCK epithelial cells[17]. Further, this study showed that β-catenin abundance and nuclear localization ~~were~~ decreased when pHi was raised, suggesting pHi acts as a rheostat to modulate β-catenin abundance and adhesion and signaling functions[17]. However, our prior work did not assess pH-

348 dependent β-catenin stability in non-epithelial models and did not characterize the
349 functional consequences of pH-dependent β-catenin stability on cell behaviors. Thus,
350 we next tested the hypothesis that stiffness-associated pHi dynamics modulate VM
351 through regulation of β-catenin abundance in metastatic cancer cell lines.

352 To determine the effect of ECM stiffening on β-catenin abundance in metastatic
353 cancer cells, we performed immunofluorescent staining of β-catenin in H1299 cells
354 plated on soft ECM and stiff ECM both with and without pHi manipulation (Figure 4A). In
355 agreement with prior work[46], we found that whole-cell abundance of β-catenin was
356 significantly increased in cells plated on stiff ECM compared to cells plated on soft ECM
357 (Figure 4B). Furthermore, we found that when we raised pHi in cells plated on stiff ECM,
358 β-catenin abundance was significantly reduced compared to control cells plated on stiff
359 ECM (Figure 4B). We also determined the effects of ECM stiffening and pHi modulation
360 on nuclear localization of β-catenin. We quantified the intensity of β-catenin within single
361 cell nuclei and found that β-catenin nuclear abundance was significantly increased on
362 stiff compared to soft ECM (Figure 4C). When pHi was raised in cells plated on a stiff
363 matrix, β-catenin nuclear intensity was significantly decreased compared to cells plated
364 on a stiff matrix in the absence of pHi manipulation (Figure 4C). These data show that
365 increased β-catenin abundance is correlated with low pHi in a human clonal metastatic
366 cancer cell line and confirm our hypothesis that β-catenin is a pH-dependent regulator
367 of stiffness-dependent vasculogenic mimicry. These data show that high pHi can
368 override mechanosensing by decreasing β-catenin abundance, suggesting that low pHi
369 functions as a necessary mediator of VM in cancer cells via stabilization of β-catenin
370 abundance.

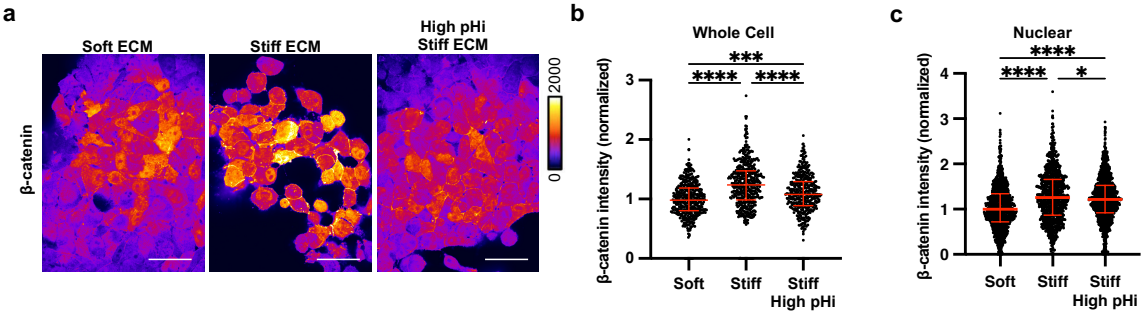


**Figure 4: Increased pHi reduced β-catenin abundance and nuclear localization in stiff matrix conditions. a)** Representative images of H1299 cells plated on soft (0.5% PEGDA), stiff (4% PEGDA) and stiff with raised pHi (4% PEGDA) HA gels fixed and stained for β-catenin. β-catenin is pseudocolored according to scale. Scale bars: 50 μm. **b)** Quantification of whole cell β-catenin intensity collected as shown in (a). (n=3 biological replicates, n=452 soft, n=486 stiff, n=415 stiff high pHi. Red lines show medians ± IQR). **c)** Quantification of nuclear β-catenin intensity collected as described in (a). (n=3 biological replicates, n=1043 soft, n=975 stiff, n=1157 stiff high. Red lines show medians ± IQR). For (b) and (c), significance was determined by a Kruskal-Wallis test (**P*<0.05; ***P*<0.01; ****P*<0. 001; *****P*<0.0001).

## FOXC2 activity is stiffness-dependent, pHi-independent, and not sufficient for vasculogenic mimicry

It is possible that other molecular regulators of VM also exhibit pHi-sensitive activity and contribute to the abrogation of stiffness-associated VM phenotypes at high pHi. Increased expression and activity of the transcription factor FOXC2 has previously been shown to promote VM in ovarian cancer[41] and breast cancer cells[48] by upregulating expression of VM associated genes. However, while FOXC2 has been shown to be required for VM[48], and sufficient to drive endothelial cell vascularization[49], it is unclear whether FOXC2 abundance or activity is a sufficient driver of VM phenotypes. Furthermore, existing literature is conflicting as to whether FOXC2 and β-catenin are independent drivers of VM. For example, significant prior data suggests that β-catenin functions upstream of FOXC2 in VM, with β-catenin being shown to directly control

395 expression of FOX transcription factors[49]. However, other data suggests that FOXC2
396 can directly induce Wnt signaling[50,51] and rescues acquisition of vasculogenic mimicry
397 when β-catenin levels are reduced[49]. Our data showing that β-catenin is a pH-
398 dependent molecular mediator of VM allows us to explore both independence and
399 crosstalk between FOXC2 and β-catenin in regulating stiffness- and pH-dependent VM
400 phenotypes.

401 We first measured FOXC2 abundance and activity in our model of metastatic
402 lung cancer cells that form VM phenotypes. We performed immunofluorescent staining
403 of FOXC2 in H1299 cells plated on soft ECM and stiff ECM and found that whole-cell
404 abundance of FOXC2 was the same in H1299 cells plated on soft vs. stiff matrix
405 (Supplemental Figure 5A,B). This suggests that whole cell abundance of FOXC2 is not
406 regulated by ECM stiffness in these cells. We next measured FOXC2 transcriptional
407 activity in single cells. We performed single-cell analysis of FOXC2 transcriptional
408 activity using a highly specific FOXC2-TAG-Puro reporter plasmid with FOXC2 specific
409 tandem repeats flanking a core DNA binding element upstream of GFP (LipExoGen,
410 see methods). Increased FOXC2 DNA binding and transcription drives increased GFP
411 fluorescence (Supplemental Figure 5C). We performed these single-cell transcriptional
412 assays in H1299 cells plated on soft ECM and on stiff ECM with and without increased
413 pHi. We found that FOXC2 activity was significantly increased in cells plated on stiff
414 ECM compared to cells plated on soft ECM, suggesting that ECM stiffening is sufficient
415 to increase FOXC2 transcriptional activity (Supplemental Figure 3D, E). However, we
416 found that FOXC2 transcriptional activity was not altered when pHi was increased on a
417 stiff matrix (Supplemental Figure 3D,E). This result demonstrates that high pHi does not

418 decrease FOXC2 activity in cells on a stiff matrix, suggesting that pHi dynamics do not
419 override stiffness-driven increases in FOXC2 activity. Furthermore, our data show that
420 high FOXC2 transcriptional activation is not a sufficient driver of VM, as high pHi
421 abrogates VM phenotypes without altering FOXC2 transcriptional activity. Our data also
422 suggest that β-catenin loss at high pHi overrides VM independently of FOXC2 activity,
423 reducing VM phenotypes even while FOXC2 transcription remains high.

424 The prior results suggest that increased pHi can override stiffness-associated VM
425 phenotypes. We next hypothesized that low pHi is a sufficient mediator of VM and that
426 lowering pHi in H1299 cells plated on soft matrix would induce stiffness-independent
427 acquisition of VM phenotypes. To directly test this hypothesis, we used an H1299 cell
428 line that is deficient in the sodium proton exchanger (H1299-NHE1 K.O., see methods).
429 This H1299-NHE1 K.O. cell line has significantly decreased pHi (7.35±0.04) compared
430 to parental H1299 (7.60±0.03) (Figure 5A). Importantly, incubating the H1299-NHE1
431 K.O. cell line with bicarbonate raised pHi to the pHi of parental H1299 (7.62±0.04)
432 Figure 5A). We performed an acid load recovery assay to confirm that the H1299-NHE1
433 K.O. cell line had no measurable NHE1 activity (Figure S6A). Using this experimental
434 system, we tested the effects of decreased pHi on modulating VM phenotypes. We
435 found that the H1299-NHE1 K.O. cells acquired a VM phenotype on soft matrix,
436 suggesting low pHi is indeed a sufficient driver of VM in the absence of stiff ECM
437 mechanical cues (Figure 5B). Importantly, the stiffness-independent VM phenotype
438 observed in H1299-NHE1 K.O. cells on soft ECM was abrogated when pHi was
439 increased in these cells on the soft matrix (Figure 5B). We again used cell area to
440 quantify extent of VM phenotype and found that when pHi is lowered (H1299-NHE1

441 K.O.) in cells plated on soft ECM, single-cell area is significantly decreased compared to
442 when the same cells plated on soft ECM but were manipulated to have a high pHi
443 (Figure 5C). Our findings demonstrate that decreased pHi is sufficient to drive VM
444 phenotype in the absence of stiffening ECM mechanical cues. Again, we confirm that
445 increasing pHi is sufficient to override VM phenotypes, even when VM is aberrantly
446 generated on soft ECM.

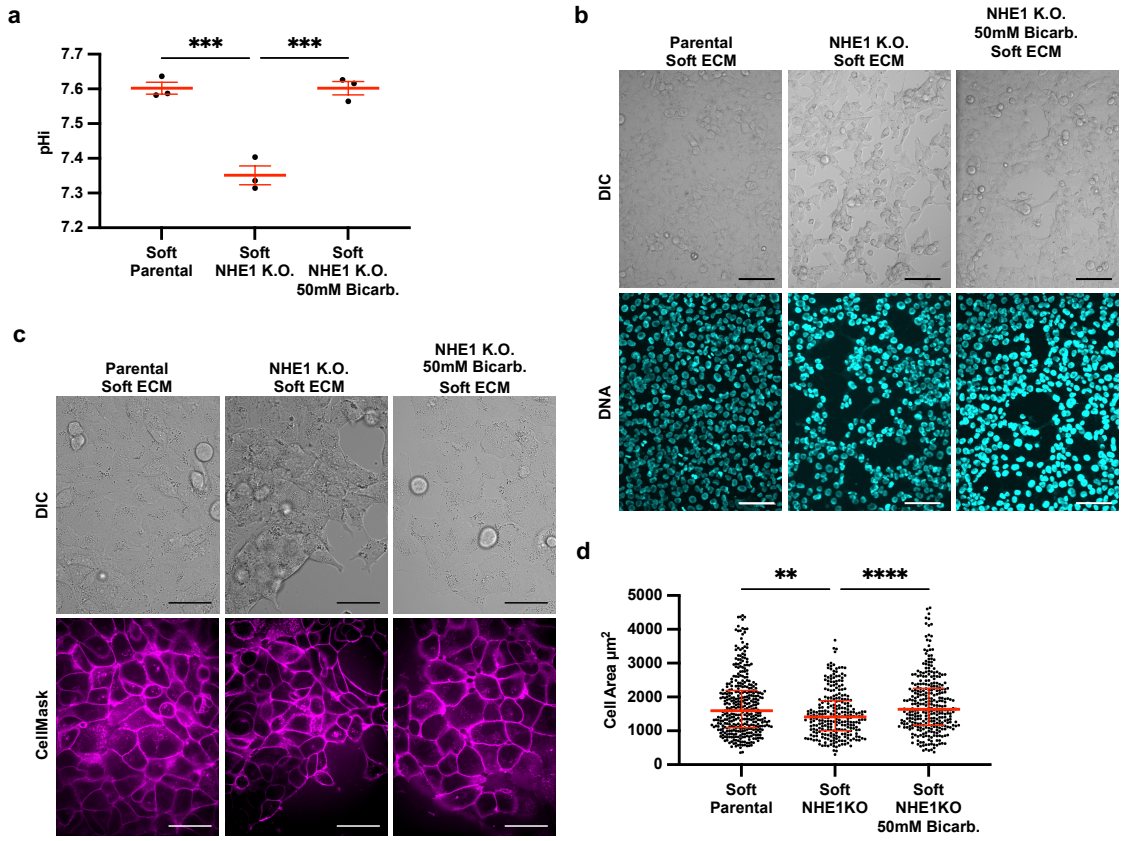


447

448 **Figure 5: Low pHi is sufficient to induce vasculogenic mimicry on a soft ECM. a)**
449 Quantification of pHi data from parental H1299 cells and H1299 cells where NHE1
450 knockout via CRISPR (H1299-NHE1 K.O.). with and without treatment with sodium
451 bicarbonate (Bicarb.) (see methods) (n=3 biological replicates. n=9 parental, n=18
452 NHE1 K.O., n=18 NHE1 K.O. Bicarb. Red lines show means ± SEM). **b)** Representative
453 images of H1299 cells plated on soft HA gels (0.5% PEGDA) with and without lowered
454 pHi (H1299-NHE1 K.O.) and with or without increased pHi (H1299-NHE1 K.O. Bicarb.).
455 Images show differential interference contrast (DIC) and Hoechst 33342 (DNA, cyan).
456 Scale bars: 100 µm. **c)** Representative images of H1299 cells plated on soft HA gels

457 (0.5% PEGDA) with and without lowered pHi (H1299-NHE1 K.O.) and with or without
458 increased pHi (H1299-NHE1 K.O. Bicarb.). Images show differential interference
459 contrast (DIC) and CellMask Deep Red membrane stain (Cy5, magenta). Scale bars: 50
460 µm. **d)** Quantification of single-cell area collected as shown in (a) (n=3 biological
461 replicates, n=383 parental, n=267 NHE1 K.O., n=315 NHE1 K.O. Bicarb. Red lines
462 show medians ± IQR).
463
464 **Discussion**

465 Our work identifies pHi dynamics as a previously unrecognized regulator of
466 stiffness-dependent VM in metastatic cancer cell models. We combined physiologically
467 relevant tunable-stiffness hydrogel systems with single-cell pHi imaging and quantitative
468 microscopy approaches to reveal novel molecular integration of the extracellular
469 mechanical environment and pHi. We show that increasing ECM stiffness, driven by
470 either increased protein concentration or crosslinking, lowers the single-cell pHi of both
471 lung and breast metastatic cell lines. Most previously described tumorigenic behaviors
472 such as hyperplasia[52], metastatic progression[34,53], and drug resistance[53] are
473 associated with increased pHi. However, recent work suggests a potential role for
474 comparatively low cancer cell pHi in regulating hypoxia response[54] and modulating
475 tumor initiating cell (or tumor stem cell) phenotypes[14]. Adding to these recent data, our
476 new findings show that low pHi in cancer cells is both a necessary and sufficient driver
477 of VM. When we raise pHi in cells plated on stiff ECM, we attenuate VM phenotypes,
478 overriding mechanosensitive regulation of VM. More surprisingly, low pHi was sufficient
479 to drive formation of VM phenotypes on soft ECM (in the absence of mechanical
480 stiffening).

481 Our work characterizing pH-dependent molecular drivers of VM identified β-
482 catenin as a pH-sensitive regulator of vasculogenic mimicry. We also show that another
483 VM regulator, FOXC2 has stiffness-dependent, but pHi-*independent*, activity. Our

484 molecular characterization of VM regulators using tunable-stiffness hydrogels in
485 combination with pHi manipulation approaches also resolved conflicting data in the
486 literature on the interdependence of β-catenin and FOXC2 in VM regulation.
487 Importantly, our data suggest that β-catenin is a necessary regulator of stiffness-
488 dependent VM and that FOXC2 transcriptional activation is not sufficient to drive VM in
489 the absence of stabilized β-catenin.

490 Our data reveal that pHi is a master regulator of VM and can override
491 mechanosensitive phenotypes in 2D, revealing an improved understanding of molecular
492 mechanisms driving cancer cell adaptive behaviors in the context of a stiffening ECM. In
493 this work, we limit our characterization to 2D ECM models and a few metastatic cell
494 models and focus on just one tumorigenic mechanosensitive phenotype (VM). This
495 approach enables us to combine single-cell pHi measurements and pHi manipulation
496 with tunable-stiffness hydrogel systems that enable differentiation of contributions of
497 stiffness and pHi in these complex cell morphology phenotypes. Our findings provide
498 the groundwork for future experiments investigating pHi-dependent mechanosensitive
499 behaviors in more complex 3D tumor spheroid models or even co-culture models with
500 cancer associated fibroblasts or immune cells. Prior work has already independently
501 shown that more complex 3D environments produce increased vasculogenic mimicry
502 and phenotypic heterogeneity[55] and pronounced pHi gradients[56]. Our current findings
503 motivate expanding these studies to more complex mechanical and cellular
504 environments to explore mechanistic roles for pHi dynamics in regulating other
505 mechanosensitive tumorigenic behaviors such as durotaxis, invasion, and phenotypic
506 plasticity (or dedifferentiation).

507

508

509 **Methods**

510 *Cell Culture*

511 H1299 (parental ATCC CRL-5803) or H1299-NHE1 K.O. (CRISPRed cell line was a gift
512 from Dr. Diane Barber at the University of California, San Francisco) were grown in
513 RPMI 1640 (Corning, 10-040-CV) supplemented with 10% Fetal Bovine Serum (FBS,
514 Peak Serum, PS-FB2).

515 MDA-MB-231 (ATCC HTB-26) cells were grown in DMEM (Corning, MT10013CVV)
516 supplemented with 10% FBS. All cells were maintained at 5% $CO_2$ and 37°C in a
517 humidified incubator. To increase pHi, cells were cultured under normal conditions for
518 24 hours before being treated for 24 hours with culture media supplemented to a final
519 concentration of 50mM Sodium Bicarbonate (Sigma-Aldrich; S6297-250G).

520

521 *Transient Expression and Stable Cell Line Generation*

522 H1299 and MDA-MB-231 mCherry-pHluorin expressing cells were generated as
523 previously described[34]. FOXC2-TAG-Puro (LipExoGen Biotech, SKU:LTV-0061)
524 positive H1299 cells were generated using lentiviral article transduction. Briefly, H1299
525 cells were plated at 50% confluency in a 6 well tissue culture treated plate. After 24
526 hours, media was replaced with fresh media containing 10ug/mL of polybrene and
527 50uL/well of FOXC2-TAG-Puro lentiviral particles. Cells were incubated for 72 hours
528 prior to selection with 0.8 mg/mL blasticidin (Thermo Fisher Scientific, BP264725). After
529 4 weeks of selection, GFP positive cells were sorted on a BD FACS ARIA III cell sorter

530 using 488nm excitation with 515nm-545nm emission filter. These cells were collected
531 into 1mL 1XPBS using high purity sort settings. Cells were then centrifuged and plated
532 in complete RPMI media with 0.8 mg/mL blasticidin.
533
534 *Preparation of tunable-stiffness hydrogels*
535 *Matrigel or Geltrex gel systems*
536 Matrigel (Corning 356231, Lot 9035003) or Geltrex (Gibco, A14132-02, add LOT)
537 coated plates were made in 35 mm diameter, 4-well (9.5 mm/well) glass bottom dishes
538 (Matsunami, D141400). Stock Matrigel or Geltrex (12 or 16 mg/mL respectively) were
539 diluted in cold complete media to concentrations of 4 mg/mL, 6 mg/mL, and 8 mg/mL
540 which cover a range of stiffness from 50 Pa to ~1000 Pa[30–32]. Each well was coated with
541 2.6 μL matrix per mm of well surface area (25 μL/well for 9.5 mm 4-well plate). Matrix
542 was allowed to solidify at 37°C for 20 minutes prior to cell plating. Cells were plated at
543 5,000 cells per well in 100 μL solution volume.
544
545 *HA gel system*
546 HyStem-C (Advanced BioMatrix GS313) gels are composed of thiol-modified hyaluronic
547 acid (Glycosil, GS222F), thiol-modified gelatin (Gelin-S, GS231F), polyethylene glycol
548 diacrylate (PEGDA, Extralink, GS3007F), and degassed, deionized water (DG
549 Water)[22,30]. Basement matrix solution was made of 1:1 Glycosil and Gelin-S and varying
550 final PEGDA percentages (0.5, 1, 2, and 4%) were prepared in degassed, deionized
551 water. The basement matrix solution and respective percentage PEGDA were mixed in
552 a 4:1 parts ratio immediately before plating. Each well was coated with 1.4 μL matrix per

553 mm of well surface area (13.5 μL/well). Cells were plated on the pre-prepared synthetic
554 ECM plates 48 hours prior to imaging at 5,000 (single-cell pHi measurements) or 75,000
555 (VM imaging/staining) cells/well in 100 μL solution volume. HA gels were pre-prepared a
556 maximum of 3 days prior to plating of cells, and stored with Dulbecco's phosphate
557 buffered saline (DPBS) (Quality Biological, 114-057-101) in each well to maintain
558 hydration at 4°C.
559
560 *Microscope System*
561 Confocal images were collected on a Nikon Ti-2 spinning disk confocal with a 10x
562 (PLAN APO NA0.45) air objective, 40x (CFI PLAN FLUOR NA1.3) oil immersion
563 objective, and 60x (PLAN APO NA1.4) oil immersion objective. The microscope is
564 equipped with a stage-top incubator (Tokai Hit), a Yokogawa spinning disk confocal
565 head (CSU-X1), four laser lines (405 nm (100 mW), 488 nm (100 mW), 561 nm (100
566 mW), 640 nm (75 mW)), a Ti2-S-SE motorized stage, multi-point perfect focus system,
567 and an Orca Flash 4.0 CMOS camera. Images were acquired under the following
568 settings: pHluorin (GFP) (488 laser excitation, 525/36 emission), mCherry (561 laser
569 excitation, 630/75 emission), Cy5 (647 nm laser excitation, 705/72 nm emission),
570 Hoechst 33342 Dye (405 nm laser excitation, 455/50 emission) and differential
571 interference contrast (DIC) were used. Acquisition times for each fluorescence channel
572 ranged from 50-600 milliseconds.
573
574 *Single-cell pHi measurements*

575 Prior to imaging, stage top incubator and microscope objectives were pre heated to
576 37°C and kept at 5% $CO_2$/95% air. Single-cell pHi measurements were performed as
577 previously described[34]. Briefly, initial fields of view (FOV) were collected on the cells in
578 their respective media. Two isotonic buffers (25 mM HEPES, 105 mM KCl, 1 mM $MgCl_2$)
579 were prepared and supplemented with 10 μM nigericin (Thermo Fisher Scientific,
580 N1495). For standardization, isotonic buffers were pre-warmed to 37°C and pH of the
581 "Nigericin buffers" was adjusted to ~6.7 and ~7.7 (with 1M KOH) (recorded for each
582 biological replicate to the hundredths place). For each standardization point, cells were
583 washed three times consecutively with no waiting time with appropriate Nigericin buffer
584 followed by a 5-7 minute equilibration prior to image acquisition. All required buffer
585 exchanges were carried out on the stage incubator to preserve XY positioning. Multiple
586 Z-planes were collected with the center focal plane maintained using the Perfect Focus
587 System (PFS).
588
589 *pHi Image Quantification*
590 NIS Analysis Software was used to quantify pHi. All images were background
591 subtracted using a region of interest (ROI) drawn on glass coverslip (determined by
592 DIC). Individual ROIs were drawn for each cell in each condition (initial, high pH
593 nigericin, and low pH nigericin). For each cell ROI, mean pHluorin and mCherry pixel
594 intensities were quantified and pHluorin/mCherry ratios calculated in Microsoft Excel.
595 For each cell, the nigericin standard fluorescence intensity values were used to
596 generate single-cell standard curves where single-cell pHi was back-calculated based
597 on nigericin buffer pH values reported to the hundredths.

598

599

600 *Proliferation Assay*

601 H1299 cells were plated at 1,000 cells/well in a 24 well tissue-culture treated plate on
602 pre-prepared matrix (65 μL/well) (see *Preparation of tunable-stiffness hydrogels*). After
603 24 and 48 hours of culture, cells were lifted via trypsinization (0.25%, Corning, 25-
604 0530CI) for 20 minutes and counted by hemocytometer.

605

606 *Immunofluorescence Staining*

607 *Fixed Cell Staining*

608 H1299 cells were plated at 75,000 cells/well in 100 μL solution volume on the pre-
609 prepared synthetic ECM plates. After 48 hours, the media was removed and a 3.7%
610 Formaldehyde (Alfa Aesar, 50-000) solution in DPBS was added to each well and
611 allowed to fix at room temperature for 10 minutes. Cells were washed 3x2 minutes with
612 DPBS before a permeabilization solution (0.1% Triton-X (Fisher Scientific, 9002-93-1) in
613 DPBS) was added to each well for ten minutes at room temperature (RT). The Triton-X
614 permeabilization solution was removed and cells were washed 3x2 minutes with DPBS
615 at RT before a blocking solution (1% BSA (Fisher Scientific, BP1600-100) was added to
616 cells for one hour at RT with rocking. The blocking solution was removed and cells were
617 washed 3x2 minutes with DPBS before primary antibody solutions were added to each
618 well and incubated with rocking at 4°C overnight. Primary antibodies were prepared in
619 1% BSA with 0.1% Triton-X at 1:50 dilutions. Primary antibodies used were: β-catenin
620 mouse (BD Biosciences, BDB610154) and FOXC2 rabbit (Cell Signaling Technology,

621 12974S). The following day, primary antibody solutions were removed and cells were
622 washed 3x2 minutes with DPBS before secondary antibodies (Goat anti-mouse IgG
623 (H+L) Cross-Absorbed Secondary Antibody, Alexa Fluor 488; Invitrogen; A-11001, Goat
624 anti-rabbit IgG (H+L) Secondary Antibody, Alexa Fluor 488; Invitrogen; A-11008) were
625 added at 1:1,000 in solution of 1% BSA, 0.1% Triton-X, and Hoechst 33342 (DAPI;
626 Thermo Scientific, cat: 62249 were added to each well (1:20,000) in DPBS and
627 incubated with rocking at RT for one hour. Cells were washed 3x2 minutes with DPBS
628 just prior to imaging on the Nikon Ti-2 spinning disk confocal with a 40x oil immersion
629 objective. Images were captured with multiple Z planes to allow visualization of labeled
630 protein colocalization. After acquisition, IMARIS Software (Bitplane, Oxford Instruments,
631 version 9.5.1) and Nikon Elements Analysis software were used to quantify stained
632 proteins. Nuclear pools of proteins were identified using IMARIS software by generating
633 surfaces based on the DAPI channel that represent individual cell nuclei. Mean
634 intensities for all channels within each nuclear surface were exported and analyzed for
635 statistical significance using GraphPad Prism software. Whole cell protein abundance
636 was determined by drawing regions of interest in Nikon Elements Analysis software of
637 single-cells. Mean intensities for all channels were exported and analyzed for statistical
638 significance using GraphPad Prism software.
639
640 *Live Cell Staining*
641 H1299 cells were plated on the pre-prepared synthetic ECM plates 48 hours prior to
642 imaging at 75,000 cells/well in 100 µL solution volume. Images were acquired as
643 outlined in the above sections. Cell nuclei and cell membranes were visualized via

644 Hoechst dye (DAPI; Thermo Scientific, cat: 62249; 1:10,000) and CellMask Deep Red
645 (Thermo Fisher, C10046; 1:20,000), respectively, incubated for 15 minutes at 37º C in
646 complete media. Fields of view were selected by visualizing nuclei (DAPI) and images
647 were collected in the DAPI (30% laser power, 600 ms), GFP (30% laser power, 600
648 ms), Cy5 (30% laser power, 600 ms), and DIC (32.6 DIA, 50 ms) channels. Individual
649 cells were analyzed by IMARIS software by generating cells based on the CellMask
650 channel that represents cell membranes. Cell areas were exported and analyzed for
651 statistical significance using GraphPad Prism software.
652
653 *Single-cell FOXC2 transcriptional activity assay using live-cell microscopy*
654 FOXC2-TAG-Puro expressing H1299 cells were plated on the pre-prepared synthetic
655 ECM plates 48 hours prior to imaging at 75,000 cells/well in 100 µL solution volume.
656 Images were acquired as outlined in the above sections. Cell nuclei and cell
657 membranes were visualized via Hoechst dye (DAPI; Thermo Scientific, cat: 62249;
658 1:10,000) and CellMask Deep Red (Thermo Fisher, C10046; 1:20,000), respectively,
659 incubated for 15 minutes at 37º C in complete media. Fields of view were selected by
660 visualizing nuclei (DAPI) and images were collected in the DAPI (30% laser power, 600
661 ms), GFP (30% laser power, 600 ms), Cy5 (30% laser power, 600 ms), and DIC (32.6
662 DIA, 50 ms) channels. Whole-cell regions of interest (ROIs) were drawn within individual
663 cells using cell mask as a membrane marker and the average GFP intensity for
664 individual cells were exported to Excel. Single-cell intensities were imported to
665 GraphPad Prism for statistical analysis and visualization.
666

667

668

669 *BCECF plate reader assays*

670 Cells were plated at 4.0×105–8.0×105 cells/well in a 24-well plate and incubated
671 overnight. Cells were treated with 2 μM 2′,7′-bis-(2-carboxyethyl)-5-(and-6)-
672 carboxyfluorescein, acetoxymethyl ester (BCECF-AM; VWR, 89139-244) for 20 min at
673 37°C and 5% $CO_2$. H1299 parental and NHE1 K.O. cells were washed three times for 5
674 min each time with a pre-warmed (37°C) HEPES-based wash buffer (30 mM HEPES pH
675 7.4, 145 mM NaCl, 5 mM KCl, 10 mM glucose, 1 mM $MgSO_4$, 1 mM $KHPO_4$, 2 mM
676 $CaCl_2$, pH 7.4) to match their low bicarbonate medium (RPMI) and NHE1 K.O. Bicarb.
677 cells were washed three times for 5 min each time with a pre-warmed (37°C) HEPES-
678 based wash buffer (30 mM HEPES pH 7.4, 95 mM NaCl, 5 mM KCl, 10 mM glucose, 1
679 mM $MgSO_4$, 1 mM $KHPO_4$, 2 mM $CaCl_2$, pH 7.4) to match sodium bicarbonate
680 treatment. For standardization, three calibration buffers (25 mM HEPES, 105 mM KCl, 1
681 mM $MgCl_2$) were supplemented with 10 μM nigericin (Thermo Fisher Scientific, N1495),
682 pH was adjusted to ~6.7, ~7.0, and ~7.7, and were pre-warmed to 37°C. Fluorescence
683 was read (excitation of 440 and 490 nm, both with emission at 535 nm) on a Cytation 5
684 (BioTek) plate reader incubated at 37°C with 5% $CO_2$. Kinetic reads were taken at 15-s
685 intervals for 5 min, using a protocol established within BioTek Gen5 software. After the
686 initial pHi read, the HEPES/bicarbonate wash was aspirated and replaced with one of
687 the nigericin buffer standards, and cells were incubated at 37°C with 5% $CO_2$ for 7 min.
688 BCECF fluorescence was read by the plate reader as above. This process was
689 repeated with the second nigericin standard. As it takes significant time to equilibrate

690 $CO_2$ in the plate reader, we did not measure nigericin standardizations without $CO_2$. The
691 mean intensity ratio (490/440 values) was derived from each read. Measurements were
692 calculated from a nigericin linear regression using exact nigericin buffer pH to two
693 decimal places (Grillo-Hill et al., 2014).
694
695 *NHE1 Recovery Assay*
696 40,000 cells were plated in the first two rows of a 24-well plate two days prior to
697 transfection (one row of H1299 parental, the other H1299 NHE1 K.O.). Cells were
698 loaded with 10uM SNARF in serum free media and incubated in the dark at 37$^o$ C for
699 30min. Each well was washed three times at 37$^o$C for 5 minutes with a HEPES buffer
700 (30mM HEPES pH-7.4, 115mM NaCl, 5mM KCl, 10mM glucose, 1mM $MgSO_4$, 1mM
701 $KHPO_4$, 2mM $CaCl_2$). The cells were imaged using a BioTek Cytation5 in imager mode.
702 The SNARF was imaged with SNARF cube (531x/586m) and TexasRed cube
703 (586x/647m). Images were taken approximately every two minutes which was the
704 shortest interval allowed by the imager mode software for two rows of a 24-well plate.
705 Initial baseline images were taken in the HEPES buffer at pH 7.4 at 3 time points
706 (approx. 6 mins total). Next, cells were loaded with ammonium chloride using a HEPES-
707 based ammonium chloride buffer (30mM HEPES pH-7.4, 30mM $NH_4Cl$, 115mM NaCl,
708 5mM KCl, 10mM glucose, 1mM $MgSO_4$, 1mM $KHPO_4$, 2mM $CaCl_2$) and cells were
709 imaged for 3 time points (approx. 6min). An acid load was induced by removing the
710 ammonium chloride buffer and replacing it with the HEPES buffer (no $NH_4Cl$) with or
711 without NHE1 inhibitor (10 μM EIPA (5-(*N*-ethyl-*N*-isopropyl) amiloride), Chemscene,
712 CS-7935). Cells were imaged while they recovered (7 time points, approx. 14 minutes).

713 A calibration curve was then obtained by imaging the cells in nigericin containing buffers
714 at the various pH's, around 7.5 (6 time points, approx. 12min), 7.0 (4 time points,
715 approx. 8min), and 6.5 (4 time points, approx. 8min). The standard curve was then used
716 to back calculate the pHi of the cells during the experiment. The data was normalized to
717 the initial point of the recovery period to look at the recovery rate.
718
719 *Statistical analysis*
720 GraphPad Prism was used to prepare graphs and perform statistical analyses. All data
721 sets were subject to normality tests (D'Angostino & Pearson, Anderson-Darling,
722 Shapiro-Wilk, and Kolmogorov-Smirnov) and outlier analyses using the ROUT method
723 (Q=1%). For non-normally distributed data, a Kruskal–Wallis test with Dunn's multiple
724 comparisons correction was used (Figures 1-5) For fold increase in cell number and
725 population pHi data, one-way ANOVA was used (Figure 2E, 5D). All significance was
726 indicated in figures by the following: *$P$<0.05; **$P$<0.01; ***$P$<0.001; ****$P$<0.0001.
727
728 **Online Supplementary Materials:** Online supplementary materials include Figure S1-
729 S6.
730
731 **Acknowledgements:** We like to thank members of the White lab for their helpful
732 conversations and feedback during figure and manuscript preparation. We also thank
733 Dr. Diane Barber for her generous gift of the H1299-NHE1 K.O. cell line. The spinning
734 disk confocal microscope used in this work is a part of the Notre Dame Integrated
735 Imaging Facility (NDIIF).

**Author contributions:** Conceptualization: LML, KAW, DH-P; Methodology: LML, KAW, LA, KJT DH-P; Validation: LML, KAW, DH-P; Formal analysis:, LML, LA, LNM, EH, JH, KJT, KAW, DH-P; Investigation: LML, LA, LNM, EH, JH; Resources: KAW, DH-P.; Data collection: LML, LA, LNM, EH, JH, KJT; Data curation: LML, LA, LNM, EH, JH, KJT, KAW, DH-P; Writing – original draft: LML, KAW; Writing - review & editing: LML, LA, LNM, EH, JH, KJT, DH-P; Visualization: LML, LNM, KAW, DH-P; Supervision: KAW, DH-P; Project administration: KAW, DH-P; Funding acquisition: LML, KAW, DH-P.

**Competing Interests:** Authors declare no competing interests.

**Funding:** This work was supported by the Walther Cancer Foundation Interdisciplinary Interface Training Project (to LML), the Henry Luce Foundation (to KAW), Harper Cancer Research Institute (to KAW & DH-P), an NIH Director's New Innovator Award (1DP2CA260416-01) (to KAW), American Cancer Society Institutional Research Grant (IRG-17-182-04 to DH-P), American Heart Association Career Development Award (19-CDA-34630012 to DH-P), National Institutes of Health (1R35-GM-143055 to DH-P).

## References

(1) Walker, C.; Mojares, E.; del Río Hernández, A. Role of Extracellular Matrix in Development and Cancer Progression. *Int. J. Mol. Sci.* **2018**, *19* (10), 3028. https://doi.org/10.3390/ijms19103028.

(2) Carey, S. P.; Martin, K. E.; Reinhart-King, C. A. Three-Dimensional Collagen Matrix Induces a Mechanosensitive Invasive Epithelial Phenotype. *Sci. Rep.* **2017**, *7* (1), 42088. https://doi.org/10.1038/srep42088.

761 (3) Wechman, S. L.; Emdad, L.; Sarkar, D.; Das, S. K.; Fisher, P. B. Vascular Mimicry:
762 Triggers, Molecular Interactions and in Vivo Models. *Adv. Cancer Res.* **2020**, *148*, 27–67.
763 https://doi.org/10.1016/bs.acr.2020.06.001.
764 (4) Webb, B. A.; Chimenti, M.; Jacobson, M. P.; Barber, D. L. Dysregulated pH: A Perfect
765 Storm for Cancer Progression. *Nat. Rev. Cancer* **2011**, *11* (9), 671–677.
766 https://doi.org/10.1038/nrc3110.
767 (5) White, K. A.; Grillo-Hill, B. K.; Barber, D. L. Cancer Cell Behaviors Mediated by
768 Dysregulated pH Dynamics at a Glance. *J. Cell Sci.* **2017**, *130* (4), 663–669.
769 https://doi.org/10.1242/jcs.195297.
770 (6) Reshkin, S. J.; Greco, M. R.; Cardone, R. A. Role of pHi, and Proton Transporters in
771 Oncogene-Driven Neoplastic Transformation. *Philos. Trans. R. Soc. B Biol. Sci.* **2014**, *369*
772 (1638), 20130100. https://doi.org/10.1098/rstb.2013.0100.
773 (7) Gilkes, D. M.; Semenza, G. L.; Wirtz, D. Hypoxia and the Extracellular Matrix: Drivers of
774 Tumour Metastasis. *Nat. Rev. Cancer* **2014**, *14* (6), 430–439.
775 https://doi.org/10.1038/nrc3726.
776 (8) Bordeleau, F.; Mason, B. N.; Lollis, E. M.; Mazzola, M.; Zanotelli, M. R.; Somasegar, S.;
777 Califano, J. P.; Montague, C.; LaValley, D. J.; Huynh, J.; Mencia-Trinchant, N.; Negrón
778 Abril, Y. L.; Hassane, D. C.; Bonassar, L. J.; Butcher, J. T.; Weiss, R. S.; Reinhart-King, C.
779 A. Matrix Stiffening Promotes a Tumor Vasculature Phenotype. *Proc. Natl. Acad. Sci. U. S.*
780 *A.* **2017**, *114* (3), 492–497. https://doi.org/10.1073/pnas.1613855114.
781 (9) DuChez, B. J.; Doyle, A. D.; Dimitriadis, E. K.; Yamada, K. M. Durotaxis by Human Cancer
782 Cells. *Biophys. J.* **2019**, *116* (4), 670–683. https://doi.org/10.1016/j.bpj.2019.01.009.
783 (10) Nallanthighal, S.; Heiserman, J. P.; Cheon, D.-J. The Role of the Extracellular Matrix in
784 Cancer Stemness. *Front. Cell Dev. Biol.* **2019**, *7*, 86.
785 https://doi.org/10.3389/fcell.2019.00086.
786 (11) Bevensee, M. O.; Boron, W. F. EFFECTS OF ACUTE HYPOXIA ON
787 INTRACELLULAR-pH REGULATION IN ASTROCYTES CULTURED FROM RAT
788 HIPPOCAMPUS. *Brain Res.* **2008**, *1193*, 143–152.
789 https://doi.org/10.1016/j.brainres.2007.12.002.
790 (12) Burbridge, M. F.; West, D. C.; Atassi, G.; Tucker, G. C. The Effect of Extracellular pH
791 on Angiogenesis in Vitro. *Angiogenesis* **1999**, *3* (3), 281–288.
792 https://doi.org/10.1023/a:1009092511894.
793 (13) Ulmschneider, B.; Grillo-Hill, B. K.; Benitez, M.; Azimova, D. R.; Barber, D. L.; Nystul,
794 T. G. Increased Intracellular pH Is Necessary for Adult Epithelial and Embryonic Stem Cell
795 Differentiation. *J. Cell Biol.* **2016**, *215* (3), 345–355. https://doi.org/10.1083/jcb.201606042.
796 (14) Liu, Y.; White, K. A.; Barber, D. L. Intracellular pH Regulates Cancer and Stem Cell
797 Behaviors: A Protein Dynamics Perspective. *Front. Oncol.* **2020**, *10*, 1401.
798 https://doi.org/10.3389/fonc.2020.01401.
799 (15) Choi, C.-H.; Webb, B. A.; Chimenti, M. S.; Jacobson, M. P.; Barber, D. L. pH Sensing
800 by FAK-His58 Regulates Focal Adhesion Remodeling. *J. Cell Biol.* **2013**, *202* (6), 849–859.
801 https://doi.org/10.1083/jcb.201302131.
802 (16) Czowski, B. J.; Romero-Moreno, R.; Trull, K. J.; White, K. A. Cancer and pH Dynamics:
803 Transcriptional Regulation, Proteostasis, and the Need for New Molecular Tools. *Cancers*
804 **2020**, *12* (10), 2760. https://doi.org/10.3390/cancers12102760.

(17) Czowski, B. J.; White, K. A. Intracellular pH Regulates β-Catenin with Low pHi Increasing Adhesion and Signaling Functions. March 27, 2024. https://doi.org/10.1101/2024.03.22.586349.
(18) Benton, G.; Arnaoutova, I.; George, J.; Kleinman, H. K.; Koblinski, J. Matrigel: From Discovery and ECM Mimicry to Assays and Models for Cancer Research. *Adv. Drug Deliv. Rev.* **2014**, *79–80*, 3–18. https://doi.org/10.1016/j.addr.2014.06.005.
(19) Kim, P. K.; Halbrook, C. J.; Kerk, S. A.; Radyk, M.; Wisner, S.; Kremer, D. M.; Sajjakulnukit, P.; Andren, A.; Hou, S. W.; Trivedi, A.; Thurston, G.; Anand, A.; Yan, L.; Salamanca-Cardona, L.; Welling, S. D.; Zhang, L.; Pratt, M. R.; Keshari, K. R.; Ying, H.; Lyssiotis, C. A. Hyaluronic Acid Fuels Pancreatic Cancer Cell Growth. *eLife 10*, e62645. https://doi.org/10.7554/eLife.62645.
(20) Deng, B.; Zhao, Z.; Kong, W.; Han, C.; Shen, X.; Zhou, C. Biological Role of Matrix Stiffness in Tumor Growth and Treatment. *J. Transl. Med.* **2022**, *20* (1), 540. https://doi.org/10.1186/s12967-022-03768-y.
(21) Fan, F.; Su, B.; Kolodychak, A.; Ekwueme, E.; Alderfer, L.; Saha, S.; Webber, M. J.; Hanjaya-Putra, D. Hyaluronic Acid Hydrogels with Phototunable Supramolecular Cross-Linking for Spatially Controlled Lymphatic Tube Formation. *ACS Appl. Mater. Interfaces* **2023**, *15* (50), 58181–58195. https://doi.org/10.1021/acsami.3c12514.
(22) Hanjaya-Putra, D.; Yee, J.; Ceci, D.; Truitt, R.; Yee, D.; Gerecht, S. Vascular Endothelial Growth Factor and Substrate Mechanics Regulate in Vitro Tubulogenesis of Endothelial Progenitor Cells. *J. Cell. Mol. Med.* **2010**, *14* (10), 2436–2447. https://doi.org/10.1111/j.1582-4934.2009.00981.x.
(23) Albeiroti, S.; Soroosh, A.; de la Motte, C. A. Hyaluronan's Role in Fibrosis: A Pathogenic Factor or a Passive Player? *BioMed Res. Int.* **2015**, *2015*, e790203. https://doi.org/10.1155/2015/790203.
(24) Nemec, S.; Ganda, S.; Al Taief, K.; Kopecky, C.; Kuchel, R.; Lebhar, H.; Marquis, C. P.; Thordarson, P.; Kilian, K. A. A Tunable Tumor Microenvironment through Recombinant Bacterial Collagen-Hyaluronic Acid Hydrogels. *ACS Appl. Bio Mater.* **2022**. https://doi.org/10.1021/acsabm.2c00186.
(25) Alderfer, L.; Russo, E.; Archilla, A.; Coe, B.; Hanjaya-Putra, D. Matrix Stiffness Primes Lymphatic Tube Formation Directed by Vascular Endothelial Growth Factor-C. *FASEB J. Off. Publ. Fed. Am. Soc. Exp. Biol.* **2021**, *35* (5), e21498. https://doi.org/10.1096/fj.202002426RR.
(26) Piersma, B.; Hayward, M.-K.; Weaver, V. M. Fibrosis and Cancer: A Strained Relationship. *Biochim. Biophys. Acta Rev. Cancer* **2020**, *1873* (2), 188356. https://doi.org/10.1016/j.bbcan.2020.188356.
(27) Cooper, J.; Giancotti, F. G. Integrin Signaling in Cancer: Mechanotransduction, Stemness, Epithelial Plasticity, and Therapeutic Resistance. *Cancer Cell* **2019**, *35* (3), 347–367. https://doi.org/10.1016/j.ccell.2019.01.007.
(28) Gan, Z.; Qin, X.; Liu, H.; Liu, J.; Qin, J. Recent Advances in Defined Hydrogels in Organoid Research. *Bioact. Mater.* **2023**, *28*, 386–401. https://doi.org/10.1016/j.bioactmat.2023.06.004.
(29) Pickup, M. W.; Mouw, J. K.; Weaver, V. M. The Extracellular Matrix Modulates the Hallmarks of Cancer. *EMBO Rep.* **2014**, *15* (12), 1243–1253. https://doi.org/10.15252/embr.201439246.

(30) Vanderhooft, J. L.; Alcoutlabi, M.; Magda, J. J.; Prestwich, G. D. Rheological Properties of Cross-Linked Hyaluronan-Gelatin Hydrogels for Tissue Engineering. *Macromol. Biosci.* **2009**, *9* (1), 20–28. https://doi.org/10.1002/mabi.200800141.
(31) Mammoto, A.; Connor, K. M.; Mammoto, T.; Yung, C. W.; Huh, D.; Aderman, C. M.; Mostoslavsky, G.; Smith, L. E. H.; Ingber, D. E. A Mechanosensitive Transcriptional Mechanism That Controls Angiogenesis. *Nature* **2009**, *457* (7233), 1103–1108. https://doi.org/10.1038/nature07765.
(32) Slater, K.; Partridge, J.; Nandivada, H.; Usa, M. Tuning the Elastic Moduli of Corning® Matrigel® and Collagen I 3D Matrices by Varying the Protein Concentration.
(33) Soofi, S. S.; Last, J. A.; Liliensiek, S. J.; Nealey, P. F.; Murphy, C. J. The Elastic Modulus of Matrigel™ as Determined by Atomic Force Microscopy. *J. Struct. Biol.* **2009**, *167* (3), 216–219. https://doi.org/10.1016/j.jsb.2009.05.005.
(34) Spear, J. S.; White, K. A. Single-Cell Intracellular pH Dynamics Regulate the Cell Cycle by Timing the G1 Exit and G2 Transition. *J. Cell Sci.* **2023**, *136* (10), jcs260458. https://doi.org/10.1242/jcs.260458.
(35) Koivusalo, M.; Welch, C.; Hayashi, H.; Scott, C. C.; Kim, M.; Alexander, T.; Touret, N.; Hahn, K. M.; Grinstein, S. Amiloride Inhibits Macropinocytosis by Lowering Submembranous pH and Preventing Rac1 and Cdc42 Signaling. *J. Cell Biol.* **2010**, *188* (4), 547–563. https://doi.org/10.1083/jcb.200908086.
(36) Grillo-Hill, B. K.; Webb, B. A.; Barber, D. L. Ratiometric Imaging of pH Probes. *Methods Cell Biol.* **2014**, *123*, 429–448. https://doi.org/10.1016/B978-0-12-420138-5.00023-9.
(37) Liu, Y.; Reyes, E.; Castillo-Azofeifa, D.; Klein, O. D.; Nystul, T.; Barber, D. L. Intracellular pH Dynamics Regulates Intestinal Stem Cell Lineage Specification. *Nat. Commun.* **2023**, *14* (1), 3745. https://doi.org/10.1038/s41467-023-39312-9.
(38) Martin, C.; Pedersen, S. F.; Schwab, A.; Stock, C. Intracellular pH Gradients in Migrating Cells. *Am. J. Physiol.-Cell Physiol.* **2011**, *300* (3), C490–C495. https://doi.org/10.1152/ajpcell.00280.2010.
(39) Williamson, S. C.; Metcalf, R. L.; Trapani, F.; Mohan, S.; Antonello, J.; Abbott, B.; Leong, H. S.; Chester, C. P. E.; Simms, N.; Polanski, R.; Nonaka, D.; Priest, L.; Fusi, A.; Carlsson, F.; Carlsson, A.; Hendrix, M. J. C.; Seftor, R. E. B.; Seftor, E. A.; Rothwell, D. G.; Hughes, A.; Hicks, J.; Miller, C.; Kuhn, P.; Brady, G.; Simpson, K. L.; Blackhall, F. H.; Dive, C. Vasculogenic Mimicry in Small Cell Lung Cancer. *Nat. Commun.* **2016**, *7*, 13322. https://doi.org/10.1038/ncomms13322.
(40) Racordon, D.; Valdivia, A.; Mingo, G.; Erices, R.; Aravena, R.; Santoro, F.; Bravo, M. L.; Ramirez, C.; Gonzalez, P.; Sandoval, A.; González, A.; Retamal, C.; Kogan, M. J.; Kato, S.; Cuello, M. A.; Osorio, G.; Nualart, F.; Alvares, P.; Gago-Arias, A.; Fabri, D.; Espinoza, I.; Sanchez, B.; Corvalán, A. H.; Pinto, M. P.; Owen, G. I. Structural and Functional Identification of Vasculogenic Mimicry in Vitro. *Sci. Rep.* **2017**, *7* (1), 6985. https://doi.org/10.1038/s41598-017-07622-w.
(41) Schnellmann, R.; Ntekoumes, D.; Choudhury, M. I.; Sun, S.; Wei, Z.; Gerecht, S. Stiffening Matrix Induces Age-Mediated Microvascular Phenotype Through Increased Cell Contractility and Destabilization of Adherens Junctions. *Adv. Sci.* **2022**, *9* (22), 2201483. https://doi.org/10.1002/advs.202201483.
(42) Delgado-Bellido, D.; Zamudio-Martínez, E.; Fernández-Cortés, M.; Herrera-Campos, A. B.; Olmedo-Pelayo, J.; Perez, C. J.; Expósito, J.; de Álava, E.; Amaral, A. T.; Valle, F. O.;

896 Diaz, A. G.; Oliver, F. J. VE-Cadherin Modulates β-Catenin/TCF-4 to Enhance
897 Vasculogenic Mimicry. *Cell Death Dis.* **2023**, *14* (2), 135. https://doi.org/10.1038/s41419-
898 023-05666-7.
899 (43) Qi, L.; Song, W.; Liu, Z.; Zhao, X.; Cao, W.; Sun, B. Wnt3a Promotes the Vasculogenic
900 Mimicry Formation of Colon Cancer via Wnt/β-Catenin Signaling. *Int. J. Mol. Sci.* **2015**, *16*
901 (8), 18564–18579. https://doi.org/10.3390/ijms160818564.
902 (44) Xu, X.; Zhang, Y.; Wang, X.; Li, S.; Tang, L. Substrate Stiffness Drives Epithelial to
903 Mesenchymal Transition and Proliferation through the NEAT1-Wnt/β-Catenin Pathway in
904 Liver Cancer. *Int. J. Mol. Sci.* **2021**, *22* (21), 12066. https://doi.org/10.3390/ijms222112066.
905 (45) Astudillo, P. Extracellular Matrix Stiffness and Wnt/β-Catenin Signaling in Physiology
906 and Disease. *Biochem. Soc. Trans.* **2020**, *48* (3), 1187–1198.
907 https://doi.org/10.1042/BST20200026.
908 (46) Sun, M.; Chi, G.; Xu, J.; Tan, Y.; Xu, J.; Lv, S.; Xu, Z.; Xia, Y.; Li, L.; Li, Y.
909 Extracellular Matrix Stiffness Controls Osteogenic Differentiation of Mesenchymal Stem
910 Cells Mediated by Integrin A5. *Stem Cell Res. Ther.* **2018**, *9* (1), 52.
911 https://doi.org/10.1186/s13287-018-0798-0.
912 (47) White, K. A.; Grillo-Hill, B. K.; Esquivel, M.; Peralta, J.; Bui, V. N.; Chire, I.; Barber, D.
913 L. β-Catenin Is a pH Sensor with Decreased Stability at Higher Intracellular pH. *J. Cell Biol.*
914 **2018**, *217* (11), 3965–3976. https://doi.org/10.1083/jcb.201712041.
915 (48) Cannell, I. G.; Sawicka, K.; Pearsall, I.; Wild, S. A.; Deighton, L.; Pearsall, S. M.; Lerda,
916 G.; Joud, F.; Khan, S.; Bruna, A.; Simpson, K. L.; Mulvey, C. M.; Nugent, F.; Qosaj, F.;
917 Bressan, D.; Dive, C.; Caldas, C.; Hannon, G. J. FOXC2 Promotes Vasculogenic Mimicry
918 and Resistance to Anti-Angiogenic Therapy. *Cell Rep.* **2023**, *42* (8).
919 https://doi.org/10.1016/j.celrep.2023.112791.
920 (49) Cha, B.; Geng, X.; Mahamud, M. R.; Fu, J.; Mukherjee, A.; Kim, Y.; Jho, E.-H.; Kim, T.
921 H.; Kahn, M. L.; Xia, L.; Dixon, J. B.; Chen, H.; Srinivasan, R. S. Mechanotransduction
922 Activates Canonical Wnt/β-Catenin Signaling to Promote Lymphatic Vascular Patterning
923 and the Development of Lymphatic and Lymphovenous Valves. *Genes Dev.* **2016**, *30* (12),
924 1454–1469. https://doi.org/10.1101/gad.282400.116.
925 (50) Koch, S. Regulation of Wnt Signaling by FOX Transcription Factors in Cancer. *Cancers*
926 **2021**, *13* (14), 3446. https://doi.org/10.3390/cancers13143446.
927 (51) Gozo, M. C.; Aspuria, P.-J.; Cheon, D.-J.; Walts, A. E.; Berel, D.; Miura, N.; Karlan, B.
928 Y.; Orsulic, S. Foxc2 Induces Wnt4 and Bmp4 Expression during Muscle Regeneration and
929 Osteogenesis. *Cell Death Differ.* **2013**, *20* (8), 1031–1042.
930 https://doi.org/10.1038/cdd.2013.34.
931 (52) Grillo-Hill, B. K.; Choi, C.; Jimenez-Vidal, M.; Barber, D. L. Increased H+ Efflux Is
932 Sufficient to Induce Dysplasia and Necessary for Viability with Oncogene Expression. *eLife*
933 **2015**, *4*, e03270. https://doi.org/10.7554/eLife.03270.
934 (53) Amith, S. R.; Wilkinson, J. M.; Fliegel, L. Assessing Na+/H+ Exchange and Cell
935 Effector Functionality in Metastatic Breast Cancer. *Biochim. Open* **2016**, *2*, 16–23.
936 https://doi.org/10.1016/j.biopen.2016.01.001.
937 (54) Hulikova, A.; Harris, A. L.; Vaughan-Jones, R. D.; Swietach, P. Regulation of
938 Intracellular pH in Cancer Cell Lines under Normoxia and Hypoxia. *J. Cell. Physiol.* **2013**,
939 *228* (4), 743–752. https://doi.org/10.1002/jcp.24221.
940 (55) Konen, J.; Summerbell, E.; Dwivedi, B.; Galior, K.; Hou, Y.; Rusnak, L.; Chen, A.;
941 Saltz, J.; Zhou, W.; Boise, L. H.; Vertino, P.; Cooper, L.; Salaita, K.; Kowalski, J.; Marcus,

942 A. I. Image-Guided Genomics of Phenotypically Heterogeneous Populations Reveals
943 Vascular Signalling during Symbiotic Collective Cancer Invasion. *Nat. Commun.* **2017**, *8*,
944 15078. https://doi.org/10.1038/ncomms15078.
945 (56) Andersen, A. P.; Flinck, M.; Oernbo, E. K.; Pedersen, N. B.; Viuff, B. M.; Pedersen, S. F.
946 Roles of Acid-Extruding Ion Transporters in Regulation of Breast Cancer Cell Growth in a
947 3-Dimensional Microenvironment. *Mol. Cancer* **2016**, *15* (1), 45.
948 https://doi.org/10.1186/s12943-016-0528-0.
949